

About the role of a sessile disconnection dipole in the shear-coupled grain boundary migration

M. Larranaga,^{1,2,*} F. Momprou,^{1,2,†} M. Legros,^{1,2,‡} and N. Combe^{1,2,§}

¹*Centre d'Elaboration de Matériaux et d'Etudes Structurales, CNRS UPR 8011,
29 rue J. Marvig, BP 94347, 31055 Toulouse cedex 4, France*

²*Université de Toulouse ; UPS ; F-31055 Toulouse, France*

(Dated: December 4, 2020)

Shear-coupled grain boundary (GB) migration has been evidenced as an effective plastic mechanism in absence of the usual intragranular dislocation activity. GB migration occurs through the nucleation and further motion of disconnections. For perfect GBs, the activation barrier for migration is dominated by the disconnection nucleation. In this study, we examine the effects of a dipole of sessile disconnections on the shear-coupled GB migration using Molecular Dynamics (MD) simulations on a $\Sigma 41[001](540)$ symmetric tilt GB in aluminum. The first effect is observed on disconnection nucleation: we show that the disconnection dipole can operate as a source of mobile disconnections. The corresponding yield stress is weakly affected but the GB migration energy barrier can be reduced by 35%. The second effect is seen on the disconnection mobility: the sessile disconnection dipole impedes the disconnection motion by repulsing or attracting it. We conclude that the influence of such dipole on the GB migration favors the nucleation of mobile disconnections on one hand but slows down their motion on the other hand.

I. INTRODUCTION

In absence of dislocation activity, grain boundary (GB) migration can become an efficient mechanism of plastic deformation^{1,2}. Especially, among all the GB-based processes, shear coupled grain boundary migration (SCGBM) is considered as the most efficient one to carry plasticity, especially at low temperature or small grain sizes³. During SCGBM, the GB migrates normally to its plane while simultaneously, the two grains shear respectively to each other in a conservative manner. SCGBM is noticeably characterized by the coupling factor, the ratio between the relative shear and the normal displacement of the GB. For a given GB, SCGBM can operate following several coupling modes, each of them characterized by a given coupling factor⁴. The SCGBM has been experimentally shown and characterized mainly using transmission and scanning electron microscopy^{1,2,5-8}. Numerically, Molecular Dynamics (MD) simulations have proved to be a relevant tools to study SCGBM: both perfect model GB and polycrystalline materials have been examined in pure metals⁹⁻¹⁵. Most of these experimental and numerical studies have investigated the coupling factor, the couplings modes and/or the mobility of the GB. More recently, SCGBM has been shown to occur through the nucleation and migration of disconnections. Disconnections are GB defects having both a step and a dislocation character¹⁶. The step character is related to the GB migration while the dislocation character (and especially the Burgers vector) is related to the relative shear between the two grains. The operation of disconnections in SCGBM has been reported in numerical studies and the link between disconnections, coupling factor and coupling modes is now established^{11,15,17-22}. Besides, there are also several experimental evidences²³⁻²⁶ of the crucial role of disconnections during SCGBM. Numerical investigations have shown that the nucleation and

the motion of disconnections (and thus the SCGBM) are thermally activated processes. Several numerical simulations have demonstrated that the disconnection nucleation is the limiting process of the migration of perfect GBs and thus dominates the GB migration energy barrier^{15,18-20,27}. While a large fraction of numerical studies has mainly been performed on perfect GBs (infinitely flat and flawless), various authors have started to investigate the effects of GB defects on the disconnection nucleation¹⁷. Indeed, real GBs contain many defects, and their presence can alter the GB migration energy barrier primarily by favoring the disconnection nucleation process. For instance, the presence of segregated vacancies or impurities favors the disconnection nucleation and thus the GB migration^{28,29}. Triple junctions can operate as disconnection sources and can strongly influence the coupling factor of the SCGBM³⁰⁻³². The interaction of a bulk dislocation with a GB can produce sessile disconnections that can operate as a source of mobile disconnections, conservatively moving with the GB in fcc, bcc and hcp metals³³⁻³⁵. Mutual interactions of mobile disconnections during the migration has also been considered and can influence the GB migration mechanism as well³⁶.

Our present study aims at giving additional insights on the role of a GB defect on the SCGBM occurring in more realistic GBs. We theoretically consider the effect of a dipole of disconnections on the SCGBM, investigating how the elementary mechanisms of the migration unfold in the presence of this defect. Our study does not only focus on the disconnection nucleation as in previous studies, we also address for the first time to our knowledge, the effect of a GB defect on the mobility of the disconnections. Beyond the effect of a disconnection dipole on the various aspects of the GB migration, our study provides significant information on the disconnection-disconnection interaction that is a central

process to understand SCGBM in real GBs. The choice to study the effect of a disconnection dipole is motivated by the fact that such defects have been observed in the $\Sigma 41[001](540)$ Al GB²⁴: the elastic field of a disconnection dipole is much more limited than the one of a single disconnection, which explains the higher probability to find this low-energy defect in real GBs.

Section II describes the system under study and the simulation methods. Section III investigates the mobile disconnection nucleation in the presence of a dipole and confirms previous results of the literature: the sessile disconnections forming the dipole can operate as a disconnections source and conservatively move with the GB. The disconnection nucleation is interpreted as a disconnection decomposition. Section IV investigates the interaction of the mobile disconnections, responsible of the GB migration, with the sessile disconnection dipole. We show that the sessile disconnections presence introduces a friction on the mobile disconnection motion.

II. SIMULATION METHOD

As a simple case, we study the migration of a symmetric tilt GB in response to an external shear deformation in an aluminum bicrystal using the molecular dynamics (MD) simulation package LAMMPS³⁷ and an embedded-atom potential (EAM)³⁸. The low-angle $\Sigma 41[001](540)$ GB has been chosen because its SCGBM has been experimentally observed and quantitatively studied²³. Fig. 1a shows a sketch of the simulation cell. The GB forms at the interface between two symmetric grains of a perfect fcc aluminum crystal misorientated relatively to each other by a 77.31° angle around the $[001]$ direction. Periodic boundary conditions are applied along the $[4\bar{5}0]$ (y axis) and $[001]$ (z axis) directions. Throughout the paper, Miller indices are expressed in grain 1 lattice coordinates. The simulation cell x (x direction along $[540]$), y , and z sizes are, respectively, 10.1, 10.4, and 3.24 nm. The cell contains 20600 atoms approximately. Two 1.7-nm-thick slabs at the top and bottom of the cell contain atoms whose relative positions are frozen onto those of the perfect lattice. The relative displacement of the slabs along the y -direction imposes a shear stress on the GB (Fig. 1a). Fig. 1b shows the equilibrium configuration of the $\Sigma 41[001](540)$ GB at 0 K seen along the $z = [001]$ direction. Two types of characteristic structural units labeled "A" and "B" in Fig. 1b form an ABBB pattern with a periodicity of 2.594 nm. Note that these structural units are just a guide to the eye. Especially, the "B" structural units have a local environment equivalent to a lightly elastically distorted fcc unit cell.

In this work, a disconnection dipole is artificially inserted in the GB following the absorption of a vacancies row (along $[001]$) and the GB reorganization after annealing at 300 K. Fig. 1c shows the atomic configuration of this dipole: two steps are observed along the GB, bordering an ABB structural units pattern. These

two steps are characterized using the methodology described in Ref. 16: two Burgers circuits around each step displayed in Fig. 1c are performed and mapped on the dichromatic pattern of Fig. 2. These Burgers circuits are constructed following the finish-start/right-hand convention, considering the step line pointing along the $[001]$ direction. For a given step, the mapping of the portion of the Burgers circuit on the perfect crystal lattice structure of grain 1 (resp. grain 2) defines a translation vector \vec{t}_{G1} (resp. \vec{t}_{G2})²⁴. The Burgers vector and step height associated of the GB step are defined by¹⁶:

$$\vec{b} = \vec{t}_{G1} - \vec{t}_{G2} \quad (1)$$

$$h = \vec{n} \cdot \frac{\vec{t}_{G1} + \vec{t}_{G2}}{2} \quad (2)$$

with \vec{n} the unit vector normal to the GB plane. From this analysis, the steps displayed in Fig. 1c are identified as two disconnections $\vec{\beta}$ and $\vec{\bar{\beta}}$ with opposite step heights and Burgers vectors. The Burgers vector and step height of β are: $\vec{b}_\beta = \frac{1}{82}[\bar{1}90]$ $h_\beta = \frac{9}{4\sqrt{41}}a_0$, a_0 the lattice parameter. The disconnections $\vec{\beta}$ and $\vec{\bar{\beta}}$ are shown in the dichromatic pattern of Fig. 2. These two disconnections are sessile in the GB plane and form a stable dipole. The disconnections $\vec{\beta}$ and $\vec{\bar{\beta}}$ have probably a very low core energy because of their very small Burgers vectors and small step height (see Fig. 2)^{24,27}. In this study, we focus on a simple case where the disconnections are straight lines: a more realistic case involving curved disconnections is out of the scope of this work.

Our simulations are in $2D + \epsilon$ dimensions: the limited size of the cell in the z -direction as well as the translational invariance along the $[001]$ direction of the atomic configuration Fig. 1c is limited by our computational capabilities required by the Nudge Elastic Band (NEB) technique used below³⁹. Despite these limitations, we report below metastable states that are not invariant along the $[001]$ direction, so that the case of non-invariant structures along $[001]$ direction can benefit from our results.

Below, we investigate and compare the SCGBM of both a perfectly flat defectless GB, referred as perfect GB (PGB) and the same GB with the disconnections dipole shown in Fig. 1c, referred as Dip-GB.

III. MOBILE DISCONNECTION NUCLEATION

A shear stress is imposed on both PGB and Dip-GB by displacing the slabs by small increments of 8×10^{-4} nm in the y (or $-y$) direction, followed by a minimization of the potential energy using a conjugate gradient algorithm. Slabs are displaced till the first GB migration occurs and then are brought back to their initial positions. Both positive and negative shear stresses are investigated. Fig. 3 shows the shear stress as a function of the slabs relative displacement d . We first discuss the positive shear displacement region of Fig. 3. For the PGB (orange curve),

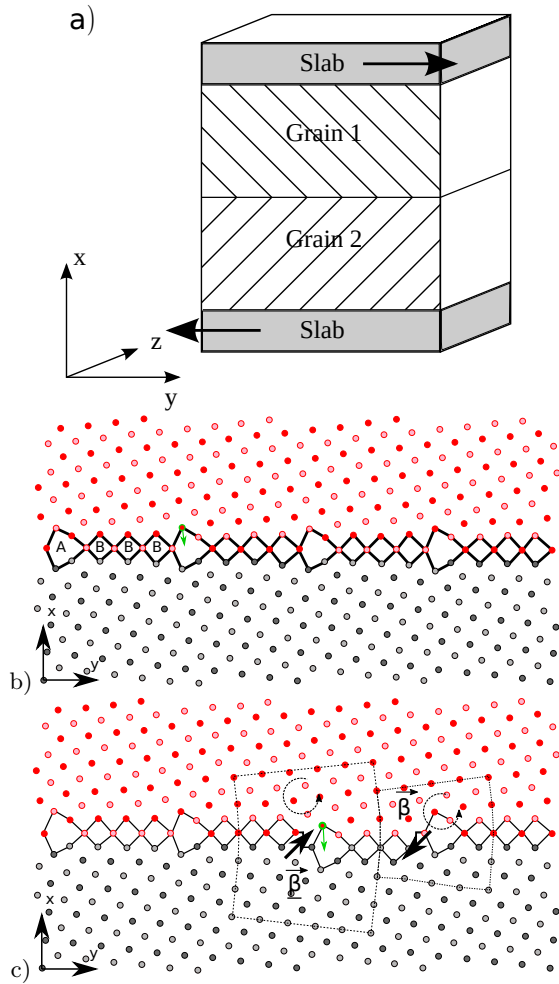


FIG. 1. (color online) a) Sketch of the simulation cell. A symmetric tilt GB perpendicular to the x-direction separates the two grains. b) Equilibrium atomic configuration of the $\Sigma 41[001](540)$ symmetric tilt GB displaying the ABBB structural units pattern. c) Structure of the studied disconnections dipole in a $\Sigma 41[001](540)$ symmetric tilt GB, Burgers vectors are represented at a scale 4:1. Black (Grey) and Red (Pink) atoms belong to different grains. Black (Red) and Grey (Pink) atoms have not the same z-coordinate. b) and c) Solid lines are guides to the eyes to display the GB. c) Dashed lines feature the circuits used to characterize the disconnections.

the shear stress first increases in the elastic regime till a shear drop happens, a plastic event corresponding to the GB migration occurring for a yield stress of 2.85 GPa at $d = 0.89$ nm. The AI EAM potential implies a slightly non linear elastic regime for $|d| > 0.3$ nm. For the Dip-GB (black curve), the shear stress increases similarly to the PGB but two shear drops are observed (see inset of Fig. 3), a first small one (of 0.02 GPa) at $d = 0.79$ nm and a second larger one (of 0.18 GPa) at $d = 0.85$ nm. The yield stress is 2.7 GPa. The yield stress is here defined as the required stress for the GB to migrate, the final GB configuration being a translation of the initial one: as shown below, two plastic events are involved in the

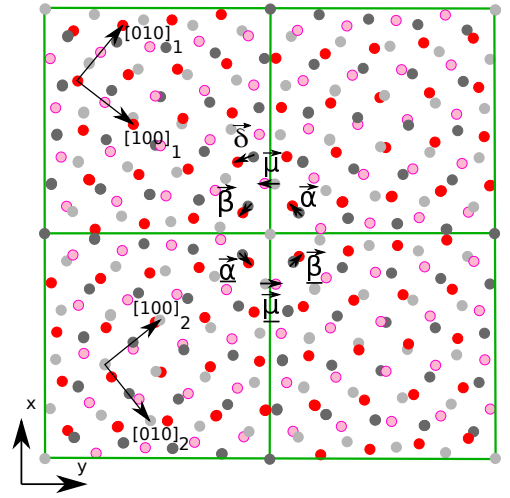


FIG. 2. (color online) a) Dichromatic pattern of the $\Sigma 41[001](540)$ symmetric tilt GB restricted to the coincident site lattice unit cell. Same color code as in Fig. 1.

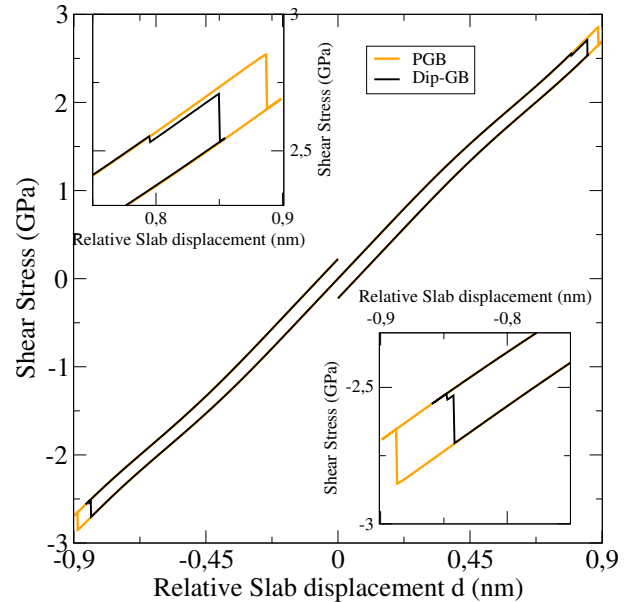


FIG. 3. (color online) Shear stress as a function of the relative slab displacement d for the PGB (orange curve) and for the Dip-GB (black). Insets display zooms of these curves in the plastic events regions.

SCGBM of the Dip-GB. Comparing both yield stress for the PGB and Dip-GB, the presence of the disconnection dipole reduces the yield stress by 5%. In order to understand the presence of the two plastic events, Fig. 1c, 4a and 4b respectively show the structures of the Dip-GB before, after the first plastic event, and after the second one. The first plastic event signed by the small stress drop at $d = 0.79$ nm, corresponds to the displacement of the ABB structural units pattern (between the disconnection dipole) observed between Fig. 1c and 4a. This displacement can also be understood using the discon-

nection formalism: the two disconnections $\vec{\beta}$ and $\underline{\vec{\beta}}$ turn to disconnections $\vec{\alpha}$ and $\underline{\vec{\alpha}}$ following the reaction

$$\vec{\beta} + \underline{\vec{\beta}} \rightarrow \vec{\alpha} + \underline{\vec{\alpha}} \quad (3)$$

Here and below, any disconnections combination also infers the conservation of the Burgers vectors and step heights, so that, Eq. (3) implies:

$$\vec{b}_\beta + \vec{b}_{\underline{\beta}} = \vec{b}_\alpha + \vec{b}_{\underline{\alpha}} \quad (4)$$

$$h_\beta + h_{\underline{\beta}} = h_\alpha + h_{\underline{\alpha}} \quad (5)$$

The transformation Eq. (3) only requires the displacement of the structural units A of the disconnection dipole (as structural units B are lightly elastically distorted fcc unit cells). Disconnections $\vec{\alpha}$ and $\underline{\vec{\alpha}}$ have opposite step heights and Burgers vectors as shown in the dichromatic pattern of Fig. 2: $\vec{b}_\alpha = \frac{1}{82}[9\bar{1}0]$ $h_\alpha = \frac{9}{4\sqrt{41}}a_0$. The second stress drop at $d = 0.85$ nm corresponds to the migration of the rest of the GB as displayed between Fig. 4a and 4b. From Fig. 1c to 4b, the GB migrates towards the x-direction while preserving its structure including the structure of the disconnection dipole. Since the first plastic event only involves part of the GB area, the intensity of the associated stress drop is dependent on the simulation cell size in the y-direction. Investigating different simulation cell sizes, we have checked that the ratio of the two shear stress drops is proportional to the ratio of the GB areas that are displaced.

The plastic events observed in the negative shear displacement region of Fig. 3 are similar. For the PGB, the plastic event corresponding to the GB migration occurs at a symmetric yield stress of -2.85 GPa and at a symmetric slab displacement $d = -0.89$ nm. Again, for the Dip-GB, two plastic events are observed: a first one involving a large stress drop (of 0.18 GPa) at $d = -0.84$ nm and a second one involving a small stress drop (of 0.02 GPa) at $d = -0.85$ nm. The yield stress is -2.70 GPa. Compared to the positive shear displacement region of Fig. 3, the order of the plastic events is reversed: a symmetric scenario operates. The first plastic event corresponds to the migration towards the (-x)-direction of the GB except for the part between the two disconnections $\vec{\beta}$ and $\underline{\vec{\beta}}$: this migration generates disconnections $\vec{\alpha}$ and $\underline{\vec{\alpha}}$ following a mechanism described below. The second plastic event corresponds to the displacement of this latter part towards the (-x)-direction: the disconnections $\vec{\beta}$ and $\underline{\vec{\beta}}$ turn to disconnections $\vec{\alpha}$ and $\underline{\vec{\alpha}}$ by the displacement of the structural unit A following the reaction $\vec{\alpha} + \underline{\vec{\alpha}} \rightarrow \vec{\beta} + \underline{\vec{\beta}}$. The net result is the displacement of the GB towards the (-x)-direction conserving its whole structure including the structure of the disconnection dipole.

For both PGB and Dip-GB, the migration occurs for an applied shear displacement d corresponding to the yield shear stress at 0 K. However, at finite temperature, the GB migration is thermally activated for smaller applied shear displacements¹⁸. In order to expose the precise atomistic mechanism of the two plastic events occurring

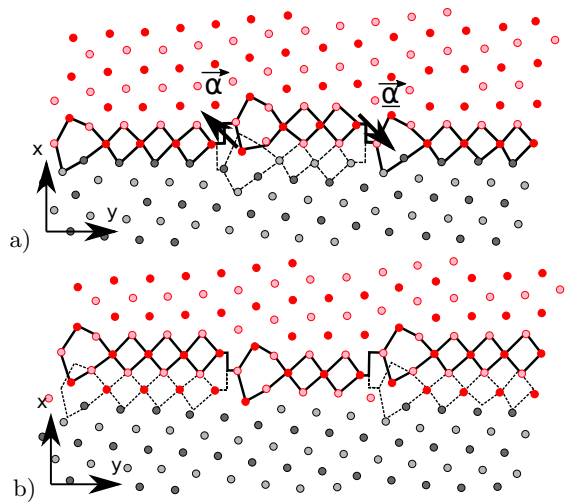


FIG. 4. (color online) Structures of Dip-GB a) after the first plastic event (at 0.79nm) and b) after the second one (at 0.85nm). Solid and dashed lines are guide to the eyes to materialize the initial GB position and its position before the last plastic event, respectively. Burgers vectors are represented at a scale 4:1.

during the Dip-GB migration, we perform NEB calculations³⁹ between atomic configurations before and after the GB migration. NEB calculations are performed both on the PGB and on the Dip-GB at constant displacement d using 505 NEB images.

Fig. 5 (orange curve) shows the Minimum Energy Path (MEP) as a function of a reaction coordinate (RC)⁴⁰ for the SCGBM of the PGB at $d = 0.05$ nm. The migration of the PGB is thermally activated. The global trend in the MEP, i.e. an initial increase in energy followed by a decrease with RC, is reminiscent of the underlying mechanism of the SCGBM i.e. the nucleation followed by the migration of mobile disconnections¹⁸. The global increase of the energy is due to the disconnection line tension, while the global decrease corresponds to the gain in elastic energy¹⁹. At a finer scale, the MEP displays oscillations in energy: we describe below the multiple metastable states deduced from a close examination of the atomic configurations along the MEP. The metastable states labeled by red arrows on the orange curve in Fig. 5 correspond to the presence of straight lines disconnections along the [001] direction. The SCGBM occurs through the nucleation and motion in opposite directions (along y) of these disconnections. A Burgers circuit analysis is performed around the nucleated disconnections: in the following, two disconnections referred as $\vec{\mu}$ and $\underline{\vec{\mu}}$ are identified and shown in the dichromatic pattern of Fig. 2: $\vec{b}_\mu = \frac{1}{41}[540]$ $h_\beta = \frac{9}{2\sqrt{41}}a_0$. The disconnections $\vec{\mu}$ and $\underline{\vec{\mu}}$ have opposite Burgers vectors and opposite step heights. These disconnections are characteristic of the $\langle 110 \rangle$ migration mode with a coupling factor of 2/9. The occurrence of the $\langle 110 \rangle$ migration mode is consistent with previous simulations performed at low temperature

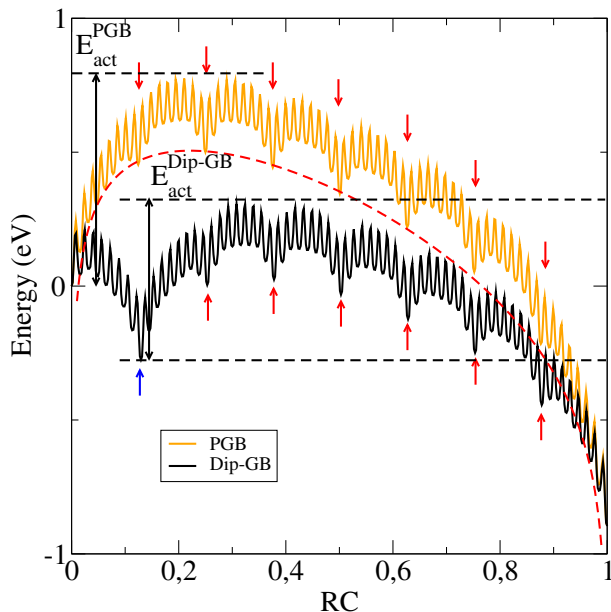


FIG. 5. (color online) Minimum Energy Path (MEP) as a function of the RC for the SCGBM of the PGB (orange curve) and of the Dip-GB (black curve) at $d = 0.05$ nm. Red and Blue arrows respectively point to configurations involving straight lines disconnections and the configuration shown in Fig. 4a. The dashed red line is a non linear fit of the energy minima (corresponding to straight line disconnections) of the PGB.

in low angle and high angle [001] tilt GBs⁹. The motion of the disconnection $\vec{\mu}$ (or $\vec{\mu}$) essentially results from the successive displacement of atoms in the atomic rows labeled by green circles in Fig. 1b towards the (-x)-direction inducing the upward displacement of the structural unit A (while the motion of structural units B does not require similar atomic displacements). These successive displacements create kinks along the disconnections lines corresponding to other metastable states in the orange curve of Fig. 5 (except at $RC = 0$ and $RC = 1$). The presence of disconnections kinks agrees with numerical observations performed on the (100) migration mode in a $\Sigma 17$ tilt GB in copper²⁰. The motion of disconnection kinks results from the displacement of a fraction of contiguous structural units A along the [001] direction: these motions are analogous to the ones described in Ref. 20.

We have fitted the straight disconnections metastable configurations energies (dashed red line on Fig. 5) by the theoretical expression $\Delta E(x) = 2E_{creation}L_z + KL_z \ln(\sin(\pi x)/\sin(\pi a_0/L_y)) + E_{stress}$ derived from the linear elasticity theory^{18,27,41}. x is the distance between mobile disconnections divided by the y-cell size L_y , L_z is z-cell size. a_0 is the aluminum lattice parameter, $E_{creation}$ is the disconnection core energy per unit length and K depends on elastic coefficient. E_{stress} is the work done by the external stress (assumed to be linear here as a function of RC). By examining the configurations along the MEP, we have checked that x is equal to RC.

We found $E_{creation} = 0.0457$ eV.nm⁻¹ and $K = 0.0739$ eV.nm⁻¹ in good agreement with previous results on similar systems¹⁸. Fig. 5 (black curve) shows the MEP as a function of RC for the SCGBM of the Dip-GB at $d = 0.05$ nm. In order to compute it, the energy landscape of the path ensemble has been widely explored: many NEB simulations have been performed changing the initial atomic configurations of NEB images. The different explored paths involve the nucleation of disconnections $\vec{\mu}$ and/or $\vec{\mu}$ at different locations (from $\vec{\alpha}$ and/or $\vec{\alpha}$, or away from them) on the GB. The MEP shown in Fig. 5 (black curve) is the energy path presenting the smallest activation energy. As in the case of the PGB, the MEP of the Dip-GB (black curve in Fig. 5) displays multiple oscillations. The atomic configuration at $RC = 0.13$ labeled by a blue arrow on Fig. 5 corresponds (regardless of elastic deformations) to the one shown in Fig. 4a: the structural units between the disconnection dipole have migrated, evidencing disconnections $\vec{\alpha}$ and $\vec{\alpha}$ while the rest of the GB has not moved. The examination of the multiple metastable states between the initial configurations $RC = 0$ and this configuration $RC = 0.13$ shows that the migration of the structural units between the disconnection dipole is performed by the nucleation and motion of kinks along disconnections $\vec{\beta}$ and $\vec{\beta}$. This disconnection migration operates similarly to the observed mechanism for the migration of disconnections in the PGB reported above i.e. through the successive displacement of atoms in the atomic row labeled by green circles in Fig. 1c towards the (-x)-direction. Using the disconnection formalism, from $RC = 0$ to $RC = 0.13$, the disconnections $\vec{\beta}$ and $\vec{\beta}$ turn to $\vec{\alpha}$ and $\vec{\alpha}$ by nucleation and migration of disconnection kinks following the reaction of Eq. 6. Note that disconnections $\vec{\beta}$ and $\vec{\beta}$ are not independent here: the displacement of the sole structural unit A between $\vec{\beta}$ and $\vec{\beta}$ induces the transformation that produces disconnections $\vec{\alpha}$ and $\vec{\alpha}$. Between $RC = 0.13$ and $RC = 1$, the MEP for the SCGBM of the Dip-GB Fig. 5 (black curve) is similar to the one of the PGB but the nucleation mechanism of the mobile disconnections differs. Between $RC = 0.13$ and 0.25 , a disconnection $\vec{\mu}$ (or $\vec{\mu}$) nucleates from disconnection $\vec{\alpha}$ following the reaction of Eq. 7.

Between $RC = 0.25$ and 1.0 , the mobile disconnection $\vec{\mu}$ migrates till it recombines with disconnection $\vec{\alpha}$ in $RC = 1$ due to periodic boundary conditions following the reaction of Eq. 8. Following this mechanism, the GB defect conservatively moves with the migrating GB. Fig. 6a displays sketches of the different steps of the SCGBM of the Dip-GB and features the different disconnections decomposition mechanisms.

$$\vec{\beta} + \vec{\beta} \rightarrow \vec{\alpha} + \vec{\alpha} \quad (6)$$

$$\vec{\alpha} \rightarrow \vec{\mu} + \vec{\beta} \quad (7)$$

$$\vec{\mu} + \vec{\alpha} \rightarrow \vec{\beta} \quad (8)$$

The periodic boundary conditions induce an artefact in this mechanism³³. We performed MD simulations with-

out such periodic conditions, and checked that once nucleated (Eq. 9 and 10), the mobile disconnection $\underline{\mu}$ migrates (in the -y-direction) till it reaches the surface of the sample or an alternative defect (such as a triple junction in a poly-crystal): the sessile disconnections $\underline{\beta}$ and $\underline{\alpha}$ remain on the GB. Shearing this latter GB configuration, the disconnection $\underline{\alpha}$ decomposes in disconnections $\underline{\mu}$ and $\underline{\beta}$ following Eq. 11. The migration of disconnection $\underline{\mu}$ (in the y-direction) finalizes the GB migration event. Without periodic boundary conditions, the successive disconnection reactions write as :

$$\underline{\beta} + \underline{\beta} \rightarrow \underline{\alpha} + \underline{\alpha} \quad (9)$$

$$\underline{\alpha} \rightarrow \underline{\mu} + \underline{\beta} \quad (10)$$

$$\underline{\alpha} \rightarrow \underline{\mu} + \underline{\beta} \quad (11)$$

Following the same procedure, the MEP for negative shear (negative value of d) is computed to reveal the atomistic mechanism of the GB migration occurring at $d = -0.84$ nm and $d = -0.85$ nm at 0 K on Fig. 3: Fig. 6b displays the sketches of the different steps of the SCGBM and Eq. 12, 13 and 14 report the successive reactions of the disconnections. The global mechanism is similar to the one found for positive values of d except that, the migration of the rest of GB occurs prior to the migration of the structural units between the disconnection dipole. The disconnection $\underline{\beta}$ (or equivalently $\underline{\beta}$) decomposes in $\underline{\mu}$ and $\underline{\alpha}$ (or $\underline{\mu}$ and $\underline{\alpha}$) Eq. 12. The mobile disconnection $\underline{\mu}$ then migrates (in the (-y-direction) till it recombines with disconnection $\underline{\beta}$ (due to periodic boundary conditions) following the reaction of Eq. 13. Finally, the disconnections $\underline{\alpha}$ and $\underline{\alpha}$ turn to $\underline{\beta}$ and $\underline{\beta}$ by displacement of the structural unit A between these two disconnections following Eq. 14.

$$\underline{\beta} \rightarrow \underline{\mu} + \underline{\alpha} \quad (12)$$

$$\underline{\mu} + \underline{\beta} \rightarrow \underline{\alpha} \quad (13)$$

$$\underline{\alpha} + \underline{\alpha} \rightarrow \underline{\beta} + \underline{\beta} \quad (14)$$

Again, without periodic boundary conditions, the mechanism is slightly modified: Eq. 15, 16 and 17 report the successive disconnection reactions. Disconnection $\underline{\beta}$ decomposes in $\underline{\mu}$ and $\underline{\alpha}$ (Eq. 15). The mobile disconnection $\underline{\mu}$ migrates (in the -y-direction) leaving behind disconnections $\underline{\alpha}$ and $\underline{\beta}$. Then disconnection $\underline{\beta}$ decomposes in disconnections $\underline{\mu}$ and $\underline{\alpha}$ (Eq. 16), and disconnection $\underline{\mu}$ migrates in the y-direction. Finally, disconnections $\underline{\alpha}$ and $\underline{\alpha}$ turn to $\underline{\beta}$ and $\underline{\beta}$ by displacement of the structural units A between the two disconnections of the dipole, following Eq. 17.

$$\underline{\beta} \rightarrow \underline{\mu} + \underline{\alpha} \quad (15)$$

$$\underline{\beta} \rightarrow \underline{\mu} + \underline{\alpha} \quad (16)$$

$$\underline{\alpha} + \underline{\alpha} \rightarrow \underline{\beta} + \underline{\beta} \quad (17)$$

Finally, in order to fully address the role of the discon-

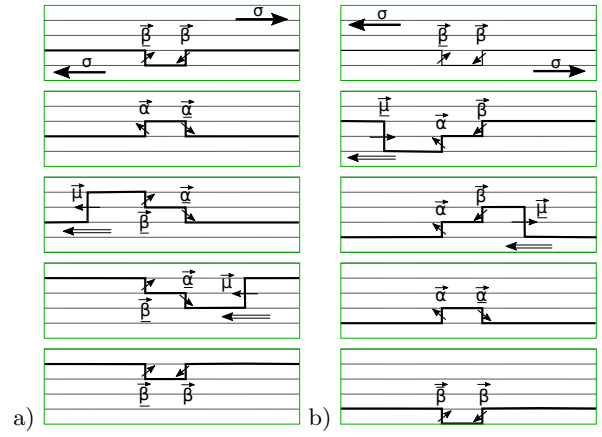


FIG. 6. (color online) Sketches of the different steps of the SCGBM of the Dip-GB for a) positive and b) negative applied shear stress in presence of periodic boundary conditions. Arrows on GB steps indicate the Burgers vectors of the disconnections. Wide and double arrows indicate the applied shear and motion direction of the mobile disconnections, respectively.

nection dipole on the disconnection nucleation process, we have computed the MEP of the SCGBM for both PGB and Dip-GB for different values of the shear displacement d . Due to the computational costs of MEP calculations, only few values of the slab displacements have been investigated. The MEP of Fig. 5 shows a multi-step reaction. Using the transition state theory⁴², we have computed the mean first passage time for the GB migration taking into account all the metastable states and energy barriers and assuming the same prefactor for all transitions. The mean first passage time follows an Arrhenius law as a function of temperature which allows to define the activation energies for the SCGBM. These activation energies E_{act}^{PGB} and E_{act}^{Dip-GB} correspond to the difference between the maximum energy along the MEP and the energy of the initial configuration (RC = 0) for the PGB and the configuration RC=0.13 for the Dip-GB (see Fig. 5). The activation energies for negative slab displacement correspond to those calculated in the positive d region. Fig. 7 shows the activation energies of the SCGBM for both PGB and Dip-GB as a function of the relative slab displacement d . As expected and as already observed in previous studies^{18,20,21,33}, activation energies decrease with applied shear displacements for both PGB and Dip-GB. Activation energies cancel for shear displacements corresponding to the SCGBM at 0 K (at the yield stress). At a given displacement, the activation energies for the Dip-GB ($d > 0$) are smaller than those of the PGB. The ratio between these activation energies could be on the order of 0.65 (obtained at $d = 0.05$ nm and $d = 0.1$ nm). This result is in agreement with recent results on similar systems³³. Overall, the presented results prove that the presence of a disconnection dipole decreases the disconnection nucleation energy barriers and confirm that sessile disconnections

can act as a source of mobile disconnections.

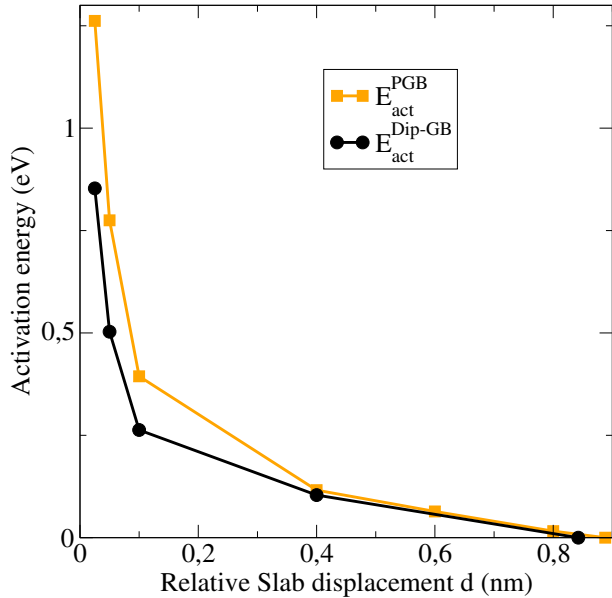


FIG. 7. (color online) Activation energies E_{act}^{PGB} and E_{act}^{Dip-GB} as a function of the relative slab displacements for both PGB and Dip-GB.

IV. DISCONNECTION MOBILITY

As mentioned before, real materials GBs commonly contain many defects that can, in principle, be involved in the nucleation of mobile disconnections. Here, we have addressed the effect of a disconnection dipole on the mobile disconnection nucleation, but other defects can alter this nucleation process, such as triple junctions, segregated vacancies, impurities, steps or dislocations. In this section we address a correlated issue: how does a sessile defect located in the path of a moving disconnection affect its mobility? Considering a material with GBs containing many defects, some mobile disconnections may nucleate from some of these defects. Once nucleated, these disconnections will migrate and potentially interact with other defects in the GB, especially because they cannot bypass them, contrary to as a dislocation that may bypass an obstacle by changing its glide plane. In this section, we address the interaction of a mobile disconnection $\vec{\mu}$ with the aforementioned disconnection dipole. Technically, we have performed NEB calculations similar to the ones performed in Sect. III except that the initial path configuration for the NEB favors the physical process that we investigate here: these NEB calculations corresponding to a minimization in the path ensemble, relax to the nearest metastable path. In such a case, the energy path resulting from the NEB is not the MEP, but rather a metastable energy path, since we consider an energy path unlikely to occur. Though artificial, this procedure gives access to the interaction of the discon-

nection $\vec{\mu}$ with the disconnection dipole. Fig. 8 shows the sketch of the investigated path: disconnections $\vec{\mu}$ and $\vec{\mu}$ homogeneously nucleate far away (at 5 nm here) from the disconnection dipole, the disconnection $\vec{\mu}$ travels and interacts with the disconnection dipole. Fig. 9a shows the computed metastable energy paths as a function of the distance $l_{\mu-\mu}$ between disconnections $\vec{\mu}$ and $\vec{\mu}$ for the Dip-GB and for the PGB (MEP of the SCGM of PGB) at $d = 0.05$ nm. The distance $l_{\mu-\mu}$ between disconnections $\vec{\mu}$ and $\vec{\mu}$ is measured on atomic configurations where disconnections are straight lines along the [001] direction and is linearly interpolated in between. The difference ΔE between the two curves of Fig. 9a is shown in Fig. 9b and investigates the interaction of disconnection $\vec{\mu}$ with the disconnections dipole $\vec{\beta}$ and $\vec{\beta}$. Fig. 9b gives an order of magnitude of the interaction between disconnection $\vec{\mu}$ and disconnections $\vec{\beta}$ and $\vec{\beta}$. We think that the oscillations (wavelength approximately 0.2 nm) displayed on Fig. 9b are presumably not physical and that only the global behavior (moving average as a blue curve of Fig. 9b) of ΔE as a function of $l_{\mu-\mu}$ is representative of a physical process. In Fig. 9a,

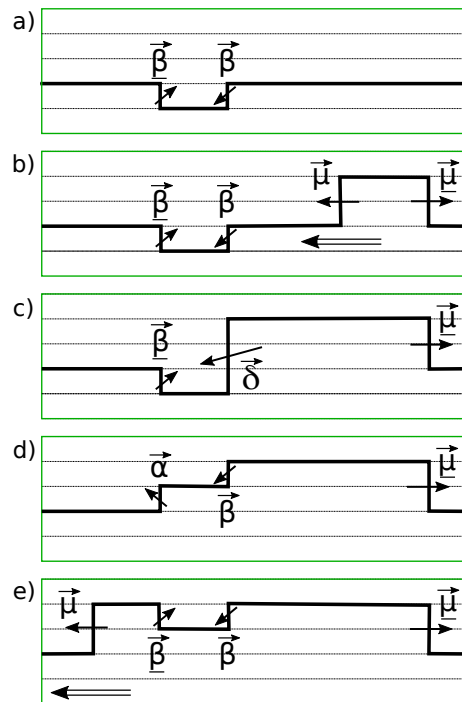


FIG. 8. (color online) Sketch of the path considered for the NEB calculations shown in the black curve of Fig. 9a

the nucleation of disconnections $\vec{\mu}$ and $\vec{\mu}$ is very similar for the PGB and the Dip-GB. The disconnection $\vec{\mu}$ then travels and repulsively interacts with disconnection $\vec{\beta}$ for $l_{\mu-\mu} < 5.1$ nm (as sketched in Fig. 8b). This repulsion is consistent with the positive scalar product of the Burgers vectors of $\vec{\mu}$ and $\vec{\beta}$. The order of magnitude of the repulsion is roughly 0.4 eV for this system, a very significant

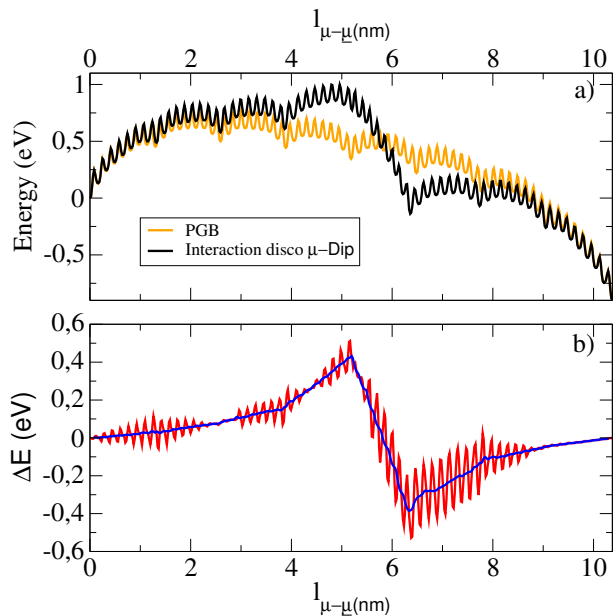


FIG. 9. (color online) a) Energy paths as a function of the distance $l_{\mu-\tilde{\mu}}$ between disconnections $\tilde{\mu}$ and μ for the SCGBM of the PGB (orange curve) and of the Dip-GB (black curve) at $d = 0.05$ nm. The disconnections $\tilde{\mu}$ and μ have nucleated far away from the disconnections dipole, and only disconnection μ migrates. b) Energy difference ΔE (red curve) between the two curves of Fig. 9a. Blue curve is an average of the red curve.

value corresponding roughly to half the nucleation activation energy E_{act}^{PGB} : the repulsion energy per unit length (along the disconnection line) is 0.12 eV.nm^{-1} . The maximum force (derivative of ΔE compared to $l_{\mu-\tilde{\mu}}$) is of the order of 0.2 eV.nm^{-1} corresponding to a repulsive stress of 0.62 eV.nm^{-2} . At $l_{\mu-\tilde{\mu}} = 5.1$ nm, $\tilde{\mu}$ combines with $\tilde{\beta}$ to produce a new disconnection $\tilde{\delta}$ as sketched in Fig. 8c: $\tilde{\mu} + \tilde{\beta} \rightarrow \tilde{\delta}$. The disconnection $\tilde{\delta}$ is shown in the dichromatic pattern of Fig. 2. Disconnections $\tilde{\delta}$ and $\tilde{\beta}$ then interact to produce $\tilde{\beta}$ and $\tilde{\alpha}$: $\tilde{\delta} + \tilde{\beta} \rightarrow \tilde{\beta} + \tilde{\alpha}$. The atomic configuration sketched in Fig. 8d precisely corresponds to the configuration at $l_{\mu-\tilde{\mu}} = 6.4$ nm. The disconnection $\tilde{\alpha}$ then decomposes in $\tilde{\beta}$ and $\tilde{\mu}$: $\tilde{\alpha} \rightarrow \tilde{\beta} + \tilde{\mu}$. The disconnection $\tilde{\beta}$ attracts $\tilde{\mu}$ in agreement with the negative scalar product of their Burgers vectors.

As a conclusion of this part, a disconnection $\tilde{\mu}$ traveling along the GB and interacting with a disconnection dipole feels a repulsion and then an attraction. The net result of this interaction is thus a friction: the motion of the disconnection is slowed down by the presence of the

sessile disconnections dipole. A mobile disconnection can even eventually be trapped by the dipole.

The interaction of the disconnection $\tilde{\mu}$, with the disconnection dipole $\tilde{\alpha} - \tilde{\alpha}$ has also been considered. An attraction and then a repulsion have been observed in agreement with the sign of the scalar product of the Burgers vectors of disconnections $\tilde{\mu}$, $\tilde{\alpha}$ and $\tilde{\alpha}$.

V. CONCLUSION

In this work, we have addressed two issues:

- The role of a GB defect on the disconnection nucleation. We have shown that a sessile disconnection dipole can operate as a disconnection source in the GB. The presence of the dipole reduces the energy barrier by about 35% for disconnection nucleation in agreement with previous findings^{33,34}. However, surprisingly, the presence of this dipole weakly affects the yield stress. We have evidenced the atomic mechanism operating during the SCGBM of the Dip-GB and shown that the disconnections dipole conservatively moves with the GB.
- The role of a GB defect on the mobility of disconnections. The presence of the disconnection dipoles induces a significant friction on the motion of a mobile disconnection and can even trap it.

The role of the disconnections dipole is thus ambivalent, on one hand, its presence favors the GB migration by being a potential source of mobile disconnections, but on the other hand, it slows it down by imposing a friction on the mobile disconnections. In every parts of our work, we have used the disconnections reactions (composition and/or decomposition): this confirms that disconnections reactions is a reliable tool to understand the role of GB defect during the SCGBM. This work contributes to the understanding of how various GB defects affect the GB migration: additional information on the effects of perfect steps⁴³, vacancies²⁹, triple junctions³¹ or impurities⁴⁴ are already available in the literature, hopefully, a theory gathering all these data in order to predict the behavior of realistic GB will emerge. Another perspective of these current studies consists in incorporating entropy effects (and thus temperature effects) in the measure of the energy barriers, i.e. computing free energy barrier⁴⁵.

This work was performed using HPC resources from CALMIP (Grant No. 2012-12172) and was funded by ANR-17-CE08-0007.

* melvyn.larranaga@cemes.fr

† mompiou@cemes.fr

‡ legros@cemes.fr

§ nicolas.combe@cemes.fr

- ¹ D. Gianola, S. V. Petegem, M. Legros, S. Brandstetter, H. V. Swygenhoven, and K. Hemker, *Acta Materialia* **54**, 2253 (2006).
- ² M. Legros, D. Gianola, and K. Hemker, *Acta Mat.* **56**, 3380 (2008).
- ³ J. Schäfer and K. Albe, *Acta Mat.* **60**, 6076 (2012).
- ⁴ J. W. Cahn, Y. Mishin, and A. Suzuki, *Phil. Mag.* **86**, 3965 (2006).
- ⁵ G. Gottstein, D. Molodov, L. Shvindlerman, D. Srolovitz, and M. Winning, *Current Opinion in Solid State and Materials Science* **5**, 9 (2001), ISSN 1359-0286.
- ⁶ F. Momprou, D. Caillard, and M. Legros, *Acta Mat.* **57**, 2198 (2009).
- ⁷ T. Gorkaya, D. A. Molodov, and G. Gottstein, *Acta mat.* **57**, 5396 (2009).
- ⁸ Q. Yu, M. Legros, and A. Minor, *MRS Bulletin* **40**, 62 (2015).
- ⁹ J. W. Cahn, Y. Mishin, and A. Suzuki, *Acta Mat.* **54**, 4953 (2006).
- ¹⁰ V. A. Ivanov and Y. Mishin, *Phys. Rev. B* **78**, 064106 (2008).
- ¹¹ L. Wan and S. Wang, *Phys. Rev. B* **82**, 214112 (2010).
- ¹² M. Velasco, H. V. Swygenhoven, and C. Brandl, *Scripta Mat.* **65**, 151 (2011).
- ¹³ Z. Trautt and Y. Mishin, *Acta Materialia* **60**, 2407 (2012).
- ¹⁴ E. R. Homer, S. M. Foiles, E. A. Holm, and D. L. Olmsted, *Acta Materialia* **61**, 1048 (2013).
- ¹⁵ K. Chen, J. Han, S. L. Thomas, and D. J. Srolovitz, *Acta Materialia* **167**, 241 (2019).
- ¹⁶ J. Hirth and R. Pond, *Acta Mat.* **44**, 4749 (1996).
- ¹⁷ H. Khater, A. Serra, R. Pond, and J. Hirth, *Acta Mat.* **60**, 2007 (2012).
- ¹⁸ A. Rajabzadeh, F. Momprou, M. Legros, and N. Combe, *Phys. Rev. Lett.* **110**, 265507 (2013).
- ¹⁹ C. P. Race, J. von Pezold, and J. Neugebauer, *Phys. Rev. B* **89**, 214110 (2014).
- ²⁰ N. Combe, F. Momprou, and M. Legros, *Phys. Rev. B* **93**, 024109 (2016).
- ²¹ N. Combe, F. Momprou, and M. Legros, *Phys. Rev. Materials* **1**, 033605 (2017).
- ²² Y. Deng and C. Deng, *Acta Materialia* **131**, 400 (2017).
- ²³ A. Rajabzadeh, M. Legros, N. Combe, F. Momprou, and D. Molodov, *Phil. Mag.* **93**, 1299 (2013).
- ²⁴ A. Rajabzadeh, F. Momprou, S. Lartigue-Korinek, N. Combe, M. Legros, and D. Molodov, *Acta Mat.* **77**, 223 (2014).
- ²⁵ Q. Zhu, G. Cao, J. Wang, C. Deng, J. Li, Z. Zhang, and S. X. Mao, *Nature Comm.* **10**, 156 (2019).
- ²⁶ Q. Zhu, S. Zhao, C. Deng, X. An, K. Song, S. Mao, and J. Wang, *Acta Materialia* **199**, 42 (2020).
- ²⁷ J. Han, S. L. Thomas, and D. J. Srolovitz, *Progress in Materials Science* **98**, 386 (2018).
- ²⁸ D. Chen, T. Ghoneim, and Y. Kulkarni, *Applied Physics Letters* **111**, 161606 (2017).
- ²⁹ D. Chen, S. Xu, and Y. Kulkarni, *Phys. Rev. Mat.* **4**, 033602 (2020).
- ³⁰ M. Aramfard and C. Deng, *Modelling Simul. Mater. Sci. Eng.* **22**, 055012 (2014).
- ³¹ S. L. Thomas, C. Wei, J. Han, Y. Xiang, and D. J. Srolovitz, *Proceedings of the National Academy of Sciences* **116**, 8756 (2019).
- ³² A. Ostapovets, A. Serra, and R. Pond, *Scripta Mat.* **172**, 149 (2019).
- ³³ N. Combe, F. Momprou, and M. Legros, *Phys. Rev. Materials* **3**, 060601 (2019).
- ³⁴ N. Kvashin, P. L. García-Müller, N. Anento, and A. Serra, *Phys. Rev. Materials* **4**, 073604 (2020).
- ³⁵ A. Serra and D. J. Bacon, *Philosophical Magazine A* **73**, 333 (1996).
- ³⁶ R. Hadian, B. Grabowski, M. W. Finnis, and J. Neugebauer, *Phys. Rev. Materials* **2**, 043601 (2018).
- ³⁷ S. J. Plimpton, *J. Comp. Phys.* **117**, 1 (1995).
- ³⁸ Y. Mishin, D. Farkas, M. J. Mehl, and D. A. Papaconstantopoulos, *Phys. Rev. B* **59**, 3393 (1999).
- ³⁹ G. Henkelman, G. Jóhannesson, and H. Jónsson, in *Progress on Theoretical Chemistry and Physics*, edited by S. D. Schwartz (Kluwer Academic Publishers, Dordrecht, 2000).
- ⁴⁰ Note1, the RC is the cumulative distance (normalized by the total cumulative distance) between adjacent replicas in the configuration space of dimension 3N with N the number of atoms.
- ⁴¹ J. P. Hirth and J. Lothe, *Theory of dislocations* (Krieger Publishing Company, Malabar, Florida, 1992).
- ⁴² E. Pollak, A. Auerbach, and P. Talkner, *Biophysical Journal* **95**, 4258 (2008).
- ⁴³ R. Hadian, B. Grabowski, C. P. Race, and J. Neugebauer, *Phys. Rev. B* **94**, 165413 (2016).
- ⁴⁴ F. Tang, D. Gianola, M. Moody, K. Hemker, and J. Cairney, *Acta Materialia* **60**, 1038 (2012).
- ⁴⁵ T. Lelièvre, M. Rousset, and G. Stoltz, *Free Energy Computations* (IMPERIAL COLLEGE PRESS, 2010).